Combustion and Flame 220 (2020) 475–487

Contents lists available at ScienceDirect

Combustion and Flame

journal homepage: www.elsevier.com/locate/combustflame

A physics-based approach to modeling real-fuel combustion chemistry – VI. Predictive kinetic models of gasoline fuels

Rui Xu[a], Chiara Saggese[a], Robert Lawson[b], Ashkan Movaghar[b], Thomas Parise[a], Jiankun Shao[a], Rishav Choudhary[a], Ji-Woong Park[c], Tianfeng Lu[c], Ronald K. Hanson[a], David F. Davidson[a], Fokion N. Egolfopoulos[b], Allen Aradi[d,*], Arjun Prakash[d], Vivek Raja Raj Mohan[d], Roger Cracknell[e], Hai Wang[a,*]

[a] Department of Mechanical Engineering, Stanford University, Stanford, CA 94305, USA
[b] Department of Aerospace and Mechanical Engineering, University of Southern California, Los Angeles, CA 90089, USA
[c] Department of Mechanical Engineering, University of Connecticut, Storrs, CT 06269, USA
[d] Shell Global Solutions US Inc., 3333 Highway 6 South, Houston TX 77082, USA
[e] Shell Global Solutions (UK), 40 Bank Street, Canary Wharf, London E14 5NR, United Kingdom

ARTICLE INFO

Article history:
Received 27 April 2020
Revised 15 July 2020
Accepted 16 July 2020
Available online 31 July 2020

Keywords:
Kinetics
Gasoline
Reaction Model
HyChem

ABSTRACT

The HyChem (hybrid chemistry) approach is utilized for modeling the combustion behaviors of gasoline fuels. The approach combines an experimentally constrained, lumped-step model for fuel pyrolysis under the high-temperature combustion condition and a detailed foundation fuel chemistry model to describe the subsequent oxidation of the pyrolysis products. We present results obtained for two Shell gasoline fuels as examples. The results show that with the parameters in the lumped reactions determined by matching the experiment time history data of key products of gasoline pyrolysis, the HyChem reaction models capture the ignition delay times and laminar flame speeds over a wide range of thermodynamic conditions. The HyChem approach is also extended to model the negative-temperature coefficient (NTC) behaviors for the gasoline fuels. The results show that the NTC-enabled models are capable of capturing the ignition delays under both high-temperature conditions and the conditions under which the NTC behaviors are important. The relationship between fuel composition and combustion properties is analyzed. Finally, the HyChem models are reduced to about 40 species to enable turbulent combustion modeling of gasoline fuels in practical engine simulations.

1. Introduction

Gasoline is petroleum product refined to attain chemical and physical properties appropriate for spark ignition (SI) engines. It is multicomponent in nature and is comprised of many classes of hydrocarbon species and may have a significant fraction of ethanol and other oxygenates added to it. The composition and properties can affect performance and emissions; and they can be of greater importance in systems that use fuel chemistry properties as control parameters of engine operation [1,2]. Historically, combustion chemistry modeling of gasoline fuels has used the surrogate fuel approach [3-10]. In this approach, a mixture of several neat components mimics the real fuel combustion and emission characteristics [11]. Examples include the primary reference fuels (PRFs) that are mixtures of *n*-heptane and *iso*-octane (2,2,4-trimethylpentane) with compositions that match the Research Octane Number (RON) or the Motor Octane Number (MON) [12-14]. Reaction kinetic models of PRFs have been developed (see, e.g., [15,16]) and used to understand the octane ratings of fuels. It was recognized later that a two-component PRF cannot fully characterize the autoignition behaviors of modern-day gasoline over a wide range of conditions [17], hence an aromatic component was added allowing the resulting toluene/PRF (TPRF) mixtures to match both the RON and MON [12]. Ignition delay times measured in shock tubes show that TPRF mixtures can reproduce real gasoline ignition properties [18,19]. Likewise, chemical kinetic calculations on TPRF mixtures are shown to predict the onset of knocking rather well [20,21].

Concerted efforts have been made on advancing multicomponent gasoline surrogate models with the addition of alkenes (e.g., 1-hexene and/or 2-pentene) [22,23] up to 10 components so as to cover a broad range of combustion chemistry behaviors [24,25]. The resulting kinetic models simulate the ignition characteristics of

* Corresponding authors.
E-mail addresses: Allen.Aradi@shell.com (A. Aradi), haiwang@stanford.edu (H. Wang).

https://doi.org/10.1016/j.combustflame.2020.07.020
0010-2180/

FACE (fuels for advanced combustion engines) that match a quite wide range of target chemical and physical properties [26]. The 10-component model has been used also to understand the combustion behaviors of high-octane gasoline with ethanol [27]. The largest chemical kinetic model for gasoline surrogates is currently available from Reaction Design [28,29]. It contains up to 20 components that span the gasoline boiling point range.

While these multi-component surrogate approaches and efforts have led to unprecedented advances in our understanding of the fuel structure-property relations, they are not without challenges. One such challenge is the requirement of extensive experimentation for developing and testing the reaction kinetic models at the individual component level. To this end, the binary, ternary and higher-order kinetic couplings of surrogate components are usually untestable because of the large number of experiments involved. The surrogate approach on its own also involves the characterization of the real-fuel combustion properties and then a comprehensive test of a proposed surrogate composition against these properties. Equally important, surrogate reaction models are usually large in size with many thermodynamic and kinetic parameters that must be estimated. They can be difficult to use in computational fluid dynamics (CFD) simulation because of their sizes even with model reduction or tabulation. For example, the reduced reaction models can still contain over 10^2 species (see, e.g., [23,30]). At this model size, high-level CFD calculations are challenging and mostly infeasible. The other problem is related to the evolving composition and properties of gasoline. With the advance of gasoline direct injection (GDI) engines and emerging alternative fuels, rapid development of compact-size, predictive combustion chemistry model has become ever more critical to facilitating gasoline fuel design and optimization.

To this end, we note that the recently proposed Hybrid Chemistry (HyChem) approach for combustion chemistry modeling of multicomponent distillate fuels [31,32] can offer an alternative path to achieve the aforementioned goal. Briefly, a HyChem model comprises an experimentally constrained lumped fuel (oxidative) pyrolysis submodel and a detailed foundational chemistry submodel that describes the oxidation of H_2/CO/C_1-C_4/benzene/toluene species. The HyChem approach has many similarities to the lumping approach championed by Ranzi and others (see, e.g., [33-35]), but it has two key differences. First, HyChem does not rely on the availability of a detailed reaction model to derive the lumped model. Rather, it relies on a physical, cause-and-effect understanding and advanced diagnostics for key products produced in fuel (oxidative) pyrolysis to derive the lumped model parameter and achieve model predictability. Additionally, the HyChem approach bypasses the use of a surrogate. It seeks to unravel the real-fuel combustion process through direct experimentation and advance the modeling capability from the measured fuel pyrolysis and oxidative pyrolysis data. Key assumptions of the HyChem approach are:

(1) High-temperature combustion of hydrocarbon fuels sufficiently large in molecular size follows a decoupled, two-step process: fuel pyrolysis first, followed by oxidation of a handful of decomposed products [31].
(2) The multicomponent nature of a real fuel simplifies the predictability of its combustion properties because of the principle of large number of fuel components, which states that when in a fuel mixture, the number of components is large enough and if the components span a sufficient number of hydrocarbon classes (i.e., paraffin, cycloparaffin and aromatics), its high-temperature combustion chemistry behavior exhibits diminishing sensitivity toward fuel composition [31,36].
(3) Fuel decomposition can be described by lumped reaction steps with constant stoichiometric coefficients and pseudo-reaction rate coefficients, which may be justified from a steady-state analysis and directly probed by time-resolved fuel pyrolysis and oxidative pyrolysis experiments in shock tube and flow reactors [31,37,38].
(4) Key pyrolysis products are relatively a few and much less diverse in composition than the initial multicomponent fuel. To date, the key species identified are C_2H_4, C_3H_6, C_4H_8 (*iso*-butene and 1-butene), CH_3, CH_4, H, H_2, C_6H_6 (benzene) and C_7H_8 (toluene). Their further reactions may be treated by detailed modeling.

The HyChem approach thus combines experimentally constrained, lumped reaction steps for fuel pyrolysis with a foundational fuel chemistry model (C_{0-4} species plus benzene and toluene) to describe the overall kinetic rate process of distillate fuel combustion. As the lumped fuel pyrolysis and oxidative pyrolysis submodel is derived from time-resolved speciation data, global combustion properties, including shock tube ignition delay times and laminar flame speeds are then used for testing model accuracy. Previously, the application of this approach to a wide range of distillate fuels, including aviation and rocket fuels [32], JP10 [39] and a bio-derived jet fuel and its blends with a conventional Jet A [40] were reported. The size of a HyChem model is compact, and can be reduced to about 30–40 species for incorporation into CFD simulations in turbulent combustors burning real jet fuels (see, e.g., [41,42]). Additionally, by incorporating again a lumped reaction model for fuel oxidation in the NTC regime, the HyChem high-temperature chemistry model has been extended to the oxidation of fuels in the intermediate and low-temperature regimes [32]. This capability is even more critical to modeling knocking in gasoline engines.

The purpose of the current work is to extend the HyChem approach by testing its applicability for gasoline fuels. Two Shell gasoline fuels are used for this purpose. Experimentally, we probe the combustion behavior of these fuels under engine relevant conditions. The combined exercise enables us to gain deeper insight into the effects of molecular compositions on the combustion properties of gasoline fuels.

2. Experimental methods

2.1. Shock tube facilities

Fuel pyrolysis speciation and ignition delay time experiments were carried out using the Stanford high-pressure (HPST) and kinetics (KST) shock tubes. Descriptions of these two facilities are provided in a recent study [43]. In brief, the high-pressure shock tube is 5.0 cm in inner diameter and uses scribed aluminum diaphragms. The low-pressure shock tube is 14.1 cm in inner diameter and uses polycarbonate diaphragms.

Three diagnostic methods were employed: pyrolysis speciation measurements via laser absorption, ignition delay time measurements via OH* emission and sidewall pressure. Laser absorption measurements took advantage of the Beer-Lambert law for fractional transmission of monochromatic light, i.e. $-ln[(I/I_0)_\lambda] = \sigma_\lambda NL$, to relate the measured absorbance $-ln[(I/I_0)_\lambda]$, with N the absorber number density and L the optical path length, to the unknown species mole fraction X, using measured absorption cross sections σ_λ. In the C_2H_4 and CH_4 time-history measurements, where one product dominates the absorbance at a particular wavelength and other species have nearly constant absorbance at this wavelength, a simple two-wavelength differential method was used to determine the concentration of the dominant absorber

Table 1
Key properties of Shell A and D fuels tested (based on detailed hydrocarbon analysis).

Fuel	Average formula	H/C ratio	O/C ratio	MW (g/mol)	Mole fraction	
					HC	Ethanol
Shell A	$C_{6.97}H_{14.36}O_{0.15}$	2.06	0.02	100.5	0.855	0.145
Shell D	$C_{6.91}H_{12.36}O_{0.12}$	1.79	0.02	97.4	0.883	0.117

[44], though more quantitative methods utilizing additional wavelengths can be applied when needed.

Experimentally determined ignition delay time values in this study are defined as the time interval from the passage of the reflected shock wave across the observation port to the time of the measured onset of pressure rise or OH* emission. This onset is determined by the inflection point of the pressure or OH* emission trace by back-extrapolating the maximum slope of the pressure or OH* emission signal linearly to the intersection with the pre-rise baseline value. For the experiments reported herein, the pressure and OH* measurements yield essentially the same results (see, e.g., Fig. S8 in the Supplementary Material).

2.2. Laminar flame speeds

Laminar flame speed, S_u^o, is measured in the counterflow configuration over a range of equivalence ratio at atmospheric pressure and an unburned mixture temperature $T_u = 373$ K. Details of the experiments are provided elsewhere [32]. Briefly, the liquid fuel is metered by a precision pump and injected into a preheated stream of air as a spray through a quartz nebulizer. A double pulsed ND:YAG laser and a 12 bit CCD camera were used to acquire Particle Image Velocimetry images. The minimum axial velocity along the system centerline just upstream of the flame is defined as a reference flame speed, $S_{u,\mathrm{ref}}$, and the maximum absolute value of axial velocity gradient is defined as a local strain rate. S_u^o is determined for each mixture through computationally-assisted extrapolation to zero stretch [45].

Flame speeds were also measured at elevated pressures in a constant volume spherical expanding flame configuration. Details of the setup can be found elsewhere [46]. The chamber, with an internal diameter of 203.2 mm, is made of stainless steel and can withstand post-combustion pressure up to 200 atm. The flame speed was determined from the measured pressure time history using the direct numerical method and a hybrid thermodynamic-radiation model. Details of the procedure are reported elsewhere [47]. The uncertainty of the laminar flame speeds (S_u^o) reported herein was quantified using an error propagation method [46], in which the combined effects of mixture preparation, data acquisition, and data post-processing were evaluated.

3. Modeling approach

3.1. Fuels tested and their properties

In the present work, two gasoline fuels were investigated: Shell A and Shell D. Key properties of the fuels, including the average molecular formulae, molecular weights, ratios of H/C and O/C, and mole fractions of ethanol and the rest of the hydrocarbon (HC) mixtures are listed in Table 1. The compositions and some basic combustion properties are also specified in Fig. 1. Both fuels contain slightly over 5% (wt) of ethanol (or about 5% ethanol by volume as in E5 gasoline). Shell A has a larger *iso*-paraffin content, while aromatics are more dominant in Shell D. The RON values of the two fuels are very close to each other, while the MON value of Shell A is slightly larger than that of Shell D. Additional fuel property data and the gas-phase thermochemical data can be found in the Supplementary Material (section S2), including the fuel compositions, sulfur contents, specific densities, and ASTM D86 boiling point curves.

For modeling purpose each fuel is represented as a "binary" mixture of ethanol and the hydrocarbon (HC) component given as C_mH_n, where m and n are taken to be integers. The determination of m and n are based on considerations of the H/C ratio and the average molecular weight of the HC component as given in Table 2. The formula of the modeled HC component is also shown in Table 2 for each fuel along with its molecular weight. The enthalpy of formation of the HC component is determined from the lower-heating value (LHV) of the fuel and ethanol, as well as the mole fractions of HC component and ethanol. The entropy and specific heat values of the HC component are estimated by using a fuel surrogate mixture that closely matches the H/C ratio, mean molecular weight, and class composition of a given fuel. Additional details about the thermochemical properties of the HC component can be found in the Supplementary material (S2). The transport properties of the modeled HC components are determined based on a series of recent studies of long-chain normal alkane molecules [48-50]. Briefly, we assume that the average binary diffusion coefficient of the HC component is equal to the diffusion coefficient of a normal alkane molecule of the same carbon number. In other words, the diffusion coefficients of Shell A and D HC components are assigned to be those of *n*-octane (*n*-C_8H_{18}). The sensitivity of the laminar flame speed to the diffusion coefficient assignment is small, as discussed in the Supplementary Materials (S3).

The use of integer molecular formula introduces some difficulties in describing the fuel combustion chemistry. In general, it is not possible to match both the equivalence ratio and mass fraction of the fuel at the same time because of small difference of the actual C/H/O ratio and the modeled C/H/O ratio. Here we take the middle ground. Specifically, using a stoichiometric Shell A-air mixture as an example, the actual complete-combustion reaction is written as

$$C_{6.97}H_{14.36}O_{0.15} + 10.49O_2 + 10.49 \times (79/21)N_2 \rightarrow 6.97CO_2 + 7.18H_2O + 10.49 \times (79/21)N_2$$

Decomposing the fuel into the HC component and ethanol, i.e., 0.855 $C_{7.82}H_{15.79}$ + 0.145 C_2H_5OH, the above formula is still exact. Replacing $C_{7.82}H_{15.79}$ by the integer formula (C_8H_{16}), we have instead 0.837 C_8H_{16} + 0.145 C_2H_5OH as the fuel mixture, where the value 0.837 comes from 0.855 × MW($C_{7.82}H_{15.79}$)/ MW(C_8H_{16}). The approach taken here is equivalent to matching the mass fraction of the fuel between experiment and simulation. Re-normalization of the mole fractions of the "binary" fuel components yields 0.852 C_8H_{16} + 0.148 C_2H_5OH, and these mole fraction values are given in the last two columns of Table 2. The conversion and renormalization of fuel mole fraction produces a 1–2% difference in the fuel C/H ratio and < 0.1% difference in the equivalence ratio. These differences yield negligible differences in the combustion property values, e.g., < 5% difference in predicted ignition delay times.

3.2. HyChem model formulation

The HyChem approach expresses the fuel pyrolysis and oxidation of the pyrolysis products as two submodels [31,32]. The oxidative pyrolysis of the HC component is modeled by experimentally constrained, lumped reaction steps. The oxidation of the HC pyrolysis products and the reaction of ethanol is described by a detailed foundational fuel chemistry model. An updated USC Mech II [40,51] with the addition of ethanol (C_2H_5OH) chemistry from Metcalfe et al. [52] is used here for this purpose. The test of the ethanol sub-chemistry has been carried out and the results are shown to be satisfactory, as seen in the Supplementary Materials (S4).

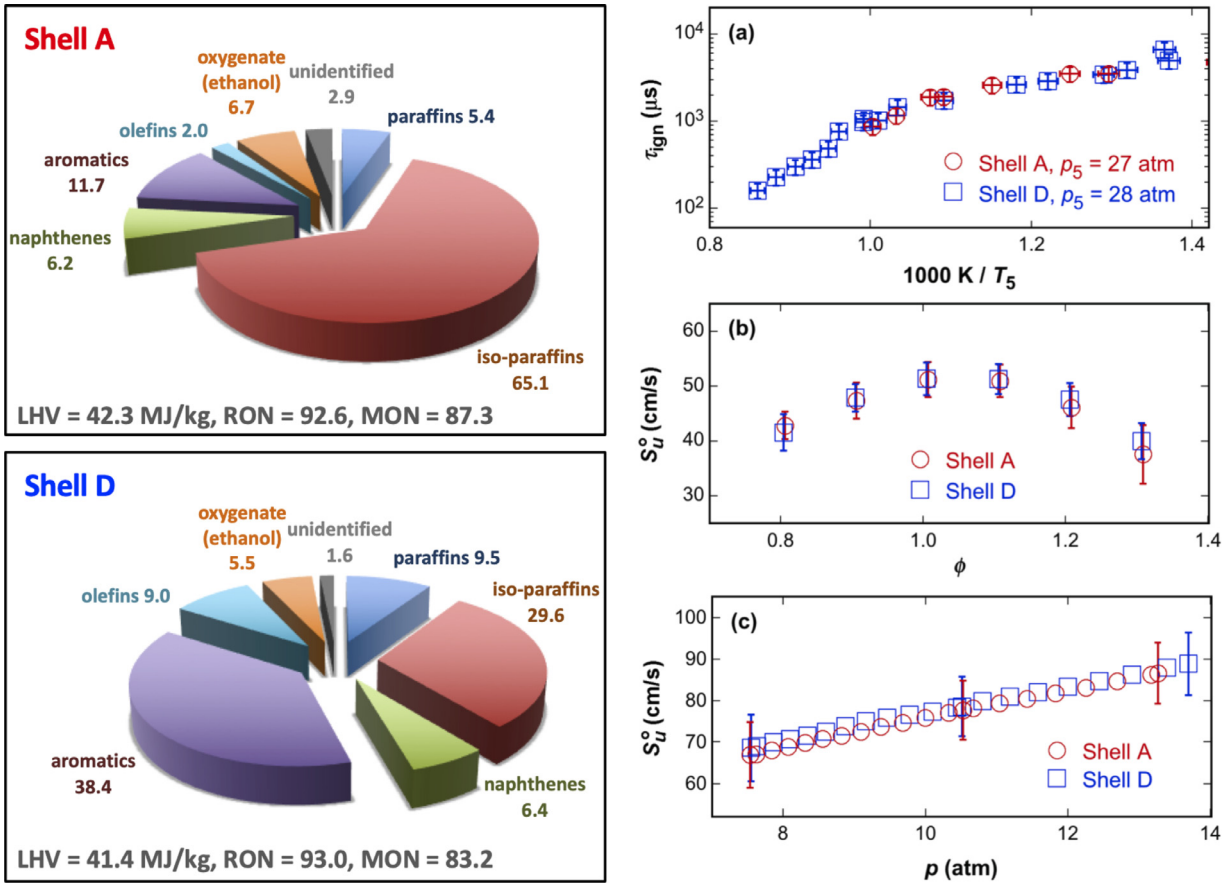

Fig. 1. Fuel compositions and basic combustion properties measured. Left column: mass percentages of the fuel components; right column: (a) shock-tube ignition delay times of fuel-air mixtures (Shell A: $\phi = 1.0$, Shell D: $\phi = 0.9$); (b) laminar flame speeds of fuel-air mixtures measured in counterflow flames at ambient pressure and unburned gas temperature of 373 K; (c) laminar flame speeds measured in constant-volume spherical flames at elevated pressures with mixture compositions (mol): 1.003 Shell A+10.49 O_2 + 25.66 N_2 + 38.49 He ($\phi = 1.003$) and 1.025 Shell D+9.94 O_2 + 24.33 N_2 + 36.50 He ($\phi = 1.025$), both with initial chamber pressure at 3 bar, and temperature at 458 K. The error bars in (b) and (c) represent 2-standard deviations of the data.

Table 2
Modeled fuel properties.

Fuel	HC component		Modeled HC component			Modeled mole fraction[a]	
	Average formula	MW (g/mol)	Name	Formula	MW (g/mol)	HC	Ethanol
Shell A	$C_{7.82}H_{15.79}$	109.8	SAC_8H_{16}	C_8H_{16}	112.2	0.852	0.148
Shell D	$C_{7.57}H_{13.20}$	104.2	SDC_8H_{14}	C_8H_{14}	110.2	0.877	0.123

[a]Slightly different from the actual values because of the use of approximate integer formula for the HC component. See text.

The stable products considered for fuel pyrolysis are ethylene (C_2H_4), propene (C_3H_6), methane (CH_4), *iso*-butene (i-C_4H_8), benzene (C_6H_6), toluene (C_7H_8), and hydrogen (H_2). The HC component lumped pyrolysis model is given in a form similar to the previous studies [31,32]:

$$C_mH_n \rightarrow e_d(C_2H_4 + \lambda_3 C_3H_6 + \lambda_{4,i} i\text{-}C_4H_8) + b_d[\chi C_6H_6 + (1-\chi)C_7H_8] + \alpha H + (2-\alpha)CH_3 \quad \text{(R1)}$$

$$C_mH_n + H \rightarrow H_2 + \Sigma_p \quad \text{(R2)}$$

$$C_mH_n + CH_3 \rightarrow CH_4 + \Sigma_p \quad \text{(R3)}$$

$$C_mH_n + OH \rightarrow H_2O + \Sigma_p \quad \text{(R4)}$$

$$C_mH_n + O_2 \rightarrow HO_2 + \Sigma_p \quad \text{(R5)}$$

$$C_mH_n + HO_2 \rightarrow H_2O_2 + \Sigma_p \quad \text{(R6)}$$

$$C_mH_n + O \rightarrow OH + \Sigma_p \quad \text{(R7)}$$

where

$$\Sigma_p = \gamma CH_4 + e_a(C_2H_4 + \lambda_3 C_3H_6 + \lambda_{4,i} i\text{-}C_4H_8) + b_a[\chi C_6H_6 + (1-\chi)C_7H_8] + \beta H + (1-\beta)CH_3$$

In the above formulations, reaction (R1) describes the "C-C fission" of the HC component, followed by the decomposition of the resulting radical fragments. Reactions (R2-R7) represent the H-abstraction of the HC component "molecule" followed by β-scission of the resulting fuel radical. There are six independent stoichiometric parameters in the lumped reaction model to be determined from experiment. They are α, β, γ, λ_3, $\lambda_{4,i}$, and χ. Their physical description, bounds and the methods of determination are

Table 3
Independent, stoichiometric parameters.

Parameter	Descriptions	Range	Method of determination
α	Number of H atoms produced in the "C–C fission reaction" (R1) per C_mH_n	[0, 2]	Fitting to shock-tube time history (C_2H_4, i-C_4H_8, C_3H_6, and CH_4)
β	Number of H atoms produced in the H-abstraction reactions (R2–7) per C_mH_n	[0, 1]	Fitting to shock-tube time history (C_2H_4, i-C_4H_8, C_3H_6, and CH_4)
γ	CH_4 yield per C_mH_n in addition to H abstraction by CH_3.[b]	$[0,\gamma_{max}]$[a]	Fitting to shock-tube time history (C_2H_4, i-C_4H_8, C_3H_6, and CH_4)
λ_3	C_3H_6 to C_2H_4 yield	[0, ∞]	Estimation from C_3H_6-to-C_2H_4 yield
$\lambda_{4,i}$	i-C_4H_8 to C_2H_4 yield	[0, ∞]	Estimation from i-C_4H_8-to-C_2H_4 yield
χ	C_6H_6 to ($C_6H_6+C_7H_8$) yield	[0,1]	Estimation from conventional distillate fuels

[a] $\gamma_{max}=[-(4-\chi)m+\frac{1}{2}(7-\chi)+3\beta]/(10-\chi)-1$. [b] γ is assumed to be zero for both Shell fuel models.

presented in Table 3. Briefly, λ_3 represents the ratio of C_3H_6-to-C_2H_4 yield; $\lambda_{4,i}$ is the ratio of i-C_4H_8-to-C_2H_4; and χ is the ratio of C_6H_6 to the sum of C_6H_6 and C_7H_8 yield. Parameter γ accounts for the yield of CH_4 in addition to its production from the H-abstraction by the CH_3 radical. In principle, the value of γ should be close to zero, as is assumed in the current work. α and β are the branching ratios of the H atom to the CH_3 radicals from reactions (R1) and (R2–7), respectively.

Stoichiometric coefficients e_d, e_a, b_d, and b_a are dependent parameters that can be determined from elemental conservations of C and H. For $\gamma=0$, we have

$$m = e_d(2+3\lambda_3+4\lambda_{4,i})+b_d(7-\chi)-\alpha+2 \tag{1}$$

$$\frac{n}{2} = e_d(2+3\lambda_3+4\lambda_{4,i})+b_d(4-\chi)-\alpha+3 \tag{2}$$

$$m = e_a(2+3\lambda_3+4\lambda_{4,i})+b_a(7-\chi)-\beta+1 \tag{3}$$

$$\frac{n}{2} = e_a(2+3\lambda_3+4\lambda_{4,i})+b_a(4-\chi)-\beta+2 \tag{4}$$

Manipulation of the above equations yields

$$e_d=\frac{1}{3}\left[-(4-\chi)m+\frac{(7-\chi)}{2}n+3\alpha+\chi-13\right]/[2+3\lambda_3+4\lambda_{4,i}], \tag{5}$$

$$e_a=\frac{1}{3}\left[-(4-\chi)m+\frac{(7-\chi)}{2}n+3\beta+\chi-10\right]/[2+3\lambda_3+4\lambda_{4,i}], \tag{6}$$

$$b_d=b_a=\frac{1}{3}\left(m-\frac{n}{2}+1\right) \tag{7}$$

The reaction rate coefficients k_i ($i=1, 2, \ldots, 7$) are estimated initially from the analogous reactions of n-octane in JetSurF [53,54]. The pyrolysis reaction rate coefficients k_{1-3}, along with α and β, are then jointly fitted to the time history data from shock tube pyrolysis experiments. The adjustments for k_{1-3} are well within a factor of 3 of the respective rate expressions of JetSurF. The lack of oxidative pyrolysis experimental data indeed created some problems with the determination of k_{4-7}. Hence, we relied on a limited number of ignition delay time data to provide further guidance in parameter determination. The validity of the model formulation and parameters are then tested against the entire sets of the ignition delay time and laminar flame speed data over a quite wide range of experimental conditions.

3.3. Simulation method

Kinetic modeling is carried out using the Sandia Chemkin code [55] for the initial value problems. The shock tube pyrolysis is simulated using the SENKIN code [56] under the adiabatic, constant pressure condition. The ignition delay time was determined as the time to reach either maximum dp/dt or maximum OH^* production rate, depending on the actual experiment, from simulations under the adiabatic, constant volume condition. In any case, the pressure and OH^* ignition criteria produce nearly identical simulation result under the conditions tested (see, e.g., Fig. S8). We chose maximum dp/dt or $d[OH^*]/dt$ rather than the inflection point, which occurs slightly earlier in reaction time, to compensate for the effect resulting from the isochoric assumption in the simulation, which produces somewhat faster reaction than isobaric reaction (see, Supplementary Material S5 for further discussion). The OH^* chemistry was taken from the SRI chemiluminescence mechanism of which the rate parameters were originated from a group of literatures [57-60]. Lastly, the laminar flame speed was calculated using PREMIX [61] with multicomponent transport and thermal diffusion.

4. Results and discussion

4.1. HyChem model derivation and testing

The stoichiometric parameters and rate coefficients of the HyChem models for gasoline fuels are constrained and determined by the speciation data obtained from the shock-tube facility. Table 4 lists the thermodynamic conditions and species measured for Shell A and D from the shock-tube facility. Representative species profiles in the shock tube pyrolysis of Shell A and D are shown in Fig. 2. As examples, Fig. 2a and c shows C_2H_4, CH_4 and i-C_4H_8 time history profiles in shock tube pyrolysis of Shell A in argon at ~1.8 and ~18 atm, respectively, each at a given initial temperature. Pyrolysis of Shell D in argon was studied at around 2 atm and results are shown in Fig. 2e and g, where C_2H_4, i-C_4H_8, C_3H_6, and CH_4 time histories are presented. These time history data were used to derive the HyChem model parameters, which are listed in Table 5. The values of $\lambda_{4,i}$ are estimated from the ratios of i-C_4H_8-to-C_2H_4 yield in the temperature range of 1100 K to 1200 K, where ethanol decomposition to C_2H_4 remains insignificant. The λ_3 value for Shell D is determined similarly; while due to the lack of C_3H_6 speciation data the same value for Shell A is estimated to be 0.5, based on the speciation data collected on a similar Shell fuel [62]. Relevant sensitivity analysis results are included in the Supplementary Materials (S6) which reveal very little effect of the λ_3 value on the ignition delay time and laminar flame speed predictions. We estimated χ to be 0.5 for both fuels (the yield of benzene and toluene being equal). The estimation is made based on earlier flow reactor studies of conventional distillate aviation fuels [31]. It will be shown later that the choice of χ has a small to negligible effect on model predictions. Stoichiometric coefficients α and β, along with

Table 4
List of shock tube experiments for Shell A and D.

Fuel	Batch No.	Species measured	Average pressure	Temperature range
Shell A	1	C_2H_4, i-C_4H_8	1.9 atm	1057 – 1215 K
	2	C_2H_4, CH_4	18.7 atm	1189 – 1333 K
Shell D	1	C_2H_4, C_3H_6, i-C_4H_8	2.0 atm	1054 – 1390 K
	2	CH_4	1.9 atm	1094 – 1325 K

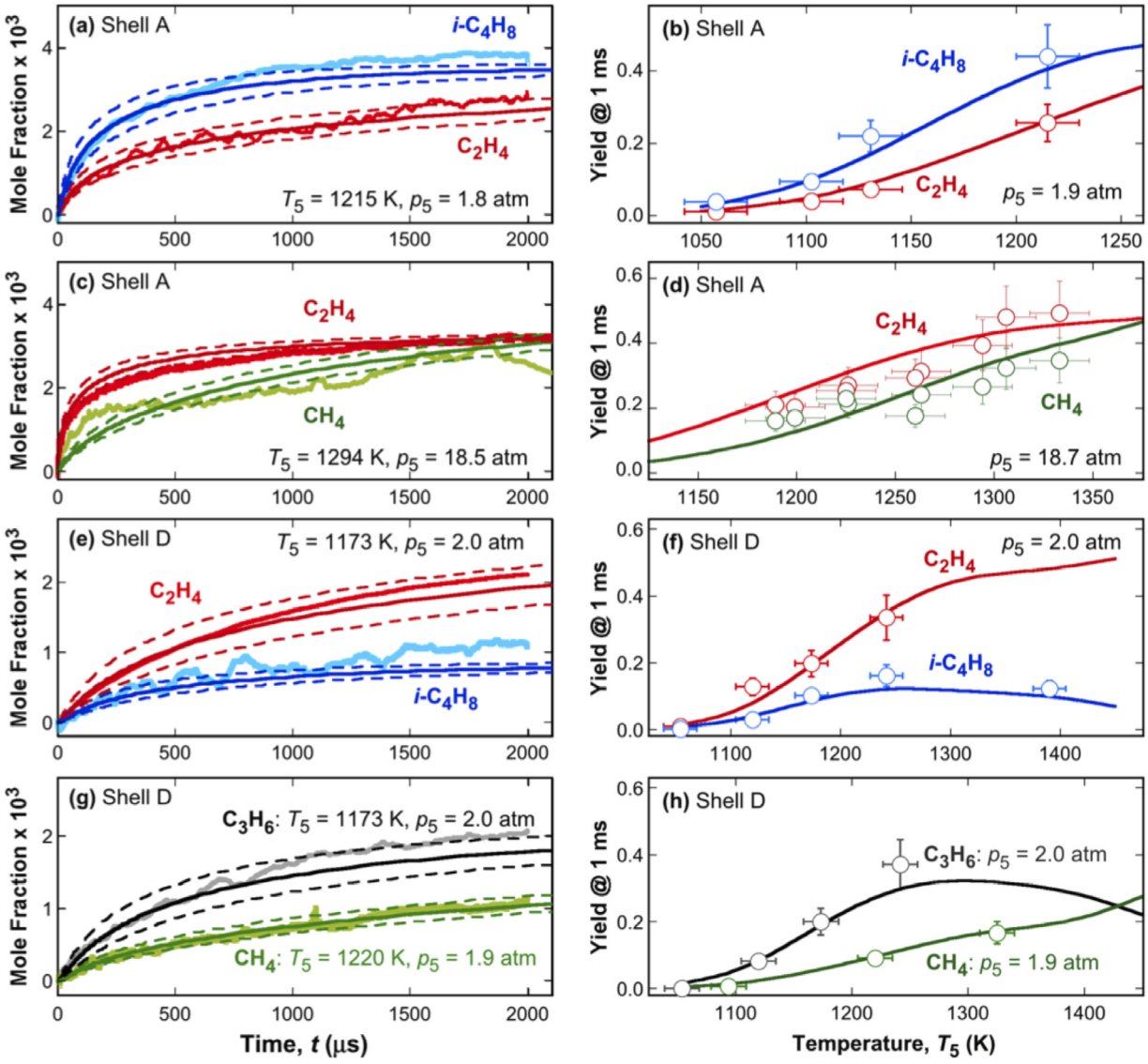

Fig. 2. Experimental (symbols) and computed (solid lines) time histories and yields of key species measured during shock tube pyrolysis of (a) & (b) 0.8% Shell A, (c) & (d) 0.7% Shell A, (e) thru (h) 0.8% Shell D, all in argon. In panels (a), (c), (e) and (g), the dashed lines represent the ± 15 K temperature sensitivity computed for the species mole fraction; in panels (b), (d), (f) and (h), the error bars represent ± 15 K of temperature uncertainty and 2-standard deviation of the measured species concentrations, and the pressure values indicated are the mean pressures of the respective experiments. See text for discussion about the various assumptions about key pyrolysis species that are not measured.

pyrolysis reaction rate coefficients k_{1-3} are jointly fitted to the time history data from shock tube pyrolysis experiments.

As shown in Fig. 2a, c, e, and g, the respective models reproduce the time histories of key species well. Summary comparisons of species yields are presented in Fig. 2b, d, f, and h at 1 ms test time over the range of T_5 tested. *Iso*-butene is the most significant pyrolysis product of Shell A, followed by ethylene and methane. For Shell D the most dominant pyrolysis products are propene and ethylene. This difference is expected to impact the respective combustion properties of the two fuels, as will be discussed later.

The models are tested against global combustion properties, including ignition delay time and laminar flame speed data, over a wide range of thermodynamic conditions. The test results are summarized in Fig. 3. Specifically, Fig. 3a and b shows measured and simulated ignition delay times of Shell A at unity equivalence ratio and three initial pressures, and of Shell D at 0.9 equivalence ratio and 28 atm initial pressure. Clearly, the models are capable of capturing the high-temperature ($T_5 > 1000$ K) experimental ignition delay time well. Without the NTC component (the solid lines), some discrepancies are found toward the lower-temperature

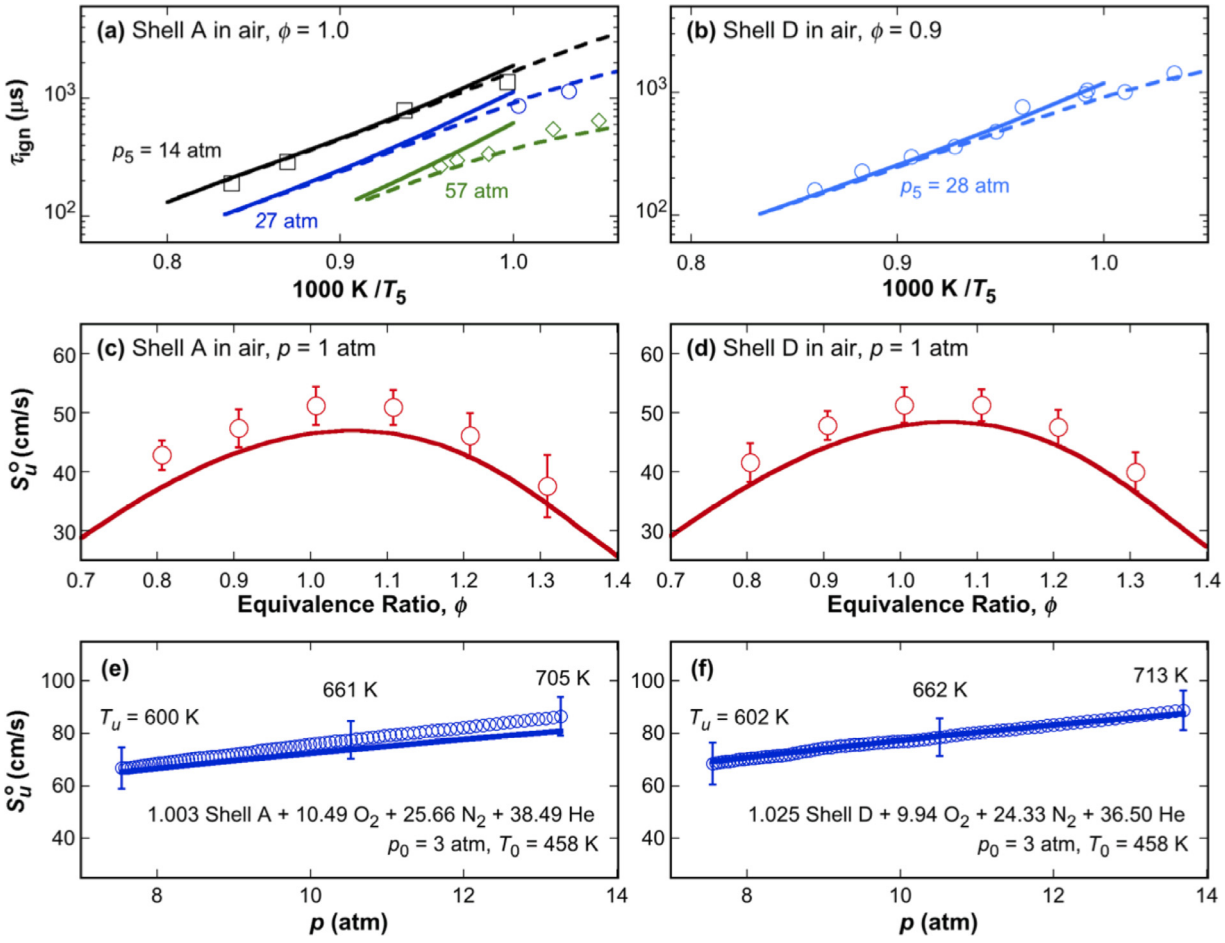

Fig. 3. Measured (symbols) and simulated (lines) (a) & (b) ignition delay times in air (solid line: high-temperature HyChem model; dashed lines: NTC-enabled HyChem model), (c) & (d) laminar flame speed in air at unburned gas temperature of 373 K and pressure of 1 atm, (e) & (f) laminar flame speeds at elevated pressures. The T_u values marked are unburned mixture temperatures, and the flame pressures are indicated by the *x*-axis. T_0 and p_0 are the initial temperature and pressure of the spherical chamber, which are not used in the simulation. The error bars on the flame speeds represent 2-standard deviations of the data.

Table 5
Model parameters of Shell A and D.

	α	β	λ_3	$\lambda_{4,i}$	χ	
Shell A	1.9	0.8	0.5	2.08	0.5	
Shell D	1.5	0.7	1.1	0.55	0.5	
$k = A\ T^n\ e^{-B/RT}$	Shell A[a]			Shell D[a]		
	A	n	B	A	n	B
k_1	3.4×10^{26}	−2.58	88.5	4.9×10^{26}	−2.58	88.5
$k_{2,\ H}$	6.3×10^{-2}	4.82	1.28	6.6×10^{-2}	4.82	1.28
$k_{3,\ CH3}$	1.8×10^{-7}	5.95	4.75	2.8×10^{-7}	5.95	4.75
$k_{4,\ OH}$	5.2×10^{8}	1.32	0	5.2×10^{8}	1.32	0
$k_{5,\ O2}$	1.5×10^{14}	0.07	47.5	1.5×10^{14}	0.07	47.5
$k_{6,\ HO2}$	3.1×10^{4}	2.94	14.9	3.1×10^{4}	2.94	14.9
$k_{7,\ O}$	3.4×10^{1}	3.93	0.72	3.4×10^{1}	3.93	0.72

[a]Units are mol, cm, s, and kcal/mol.

region. These discrepancies are resolved by introducing the NTC component into the HyChem models (shown by the dashed lines in Fig. 3a and b) as will be presented later.

The HyChem models also capture the laminar flame speeds measured both at the atmospheric (Fig. 3c and d) and elevated-pressure (Fig. 3e and f) conditions. In general, the model predictions lie close to or within the 2σ uncertainties of the data. Slight underprediction of the experimental data is observed for Shell A. The discrepancy is probably the result of inaccuracy in the *iso*-butene chemistry of USC Mech II. Since *iso*-butene is a more dominant pyrolytic product from Shell A than Shell D, a larger discrepancy is expected for Shell A than Shell D. Similar discrepancies have been also observed for a bio-derived jet fuel where *iso*-butene was also observed to be a key pyrolysis product [40]. Another potential cause for the discrepancy observed at high pressures could be our insufficient understanding of the Chaperon efficiency of He [32].

Sensitivity analysis is performed for Shell A for both atmospheric and elevated pressure flame speeds under representative experimental conditions. As seen in Fig. 4, the lumped, fuel-specific reactions do not play appreciable roles under all conditions tested. The most important reactions, as usual, are $H + O_2 = OH + O$ and $CO + OH = CO_2 + H$. Additionally, the sensitivity coefficients of $H + O_2\ (+M) = HO_2\ (+M)$ and $CH_3 + H\ (+M) = CH_4\ (+M)$ reactions are noticeably larger at 10.5 atm than at 1 atm.

4.2. NTC-enabled HyChem model

NTC chemistry is essential to gasoline applications. For this reason, the HyChem models are extended to model NTC and low-temperature oxidation in a manner similar to our jet fuel study [32]. The NTC submodel is based on Bikas and Peters [63]. A 6-species, 8-step lumped NTC reaction model is added to the high-temperature HyChem model. Since the radical β-scission becomes slow towards the NTC region, reactions (R2–7) are de-lumped into two separate steps:

$$C_mH_n + R \rightarrow RH + C_mH_{n-1} \quad \text{(R2a)}$$

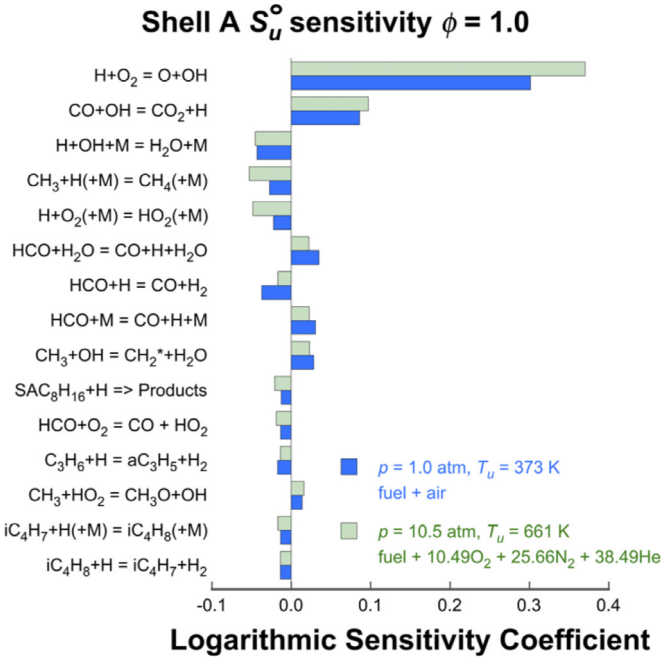

Fig. 4. Ranked logarithmic sensitivity coefficients of the laminar flame speeds of Shell A at the equivalence ratio of 1.0 and pressures of 1 and 10.5 atm.

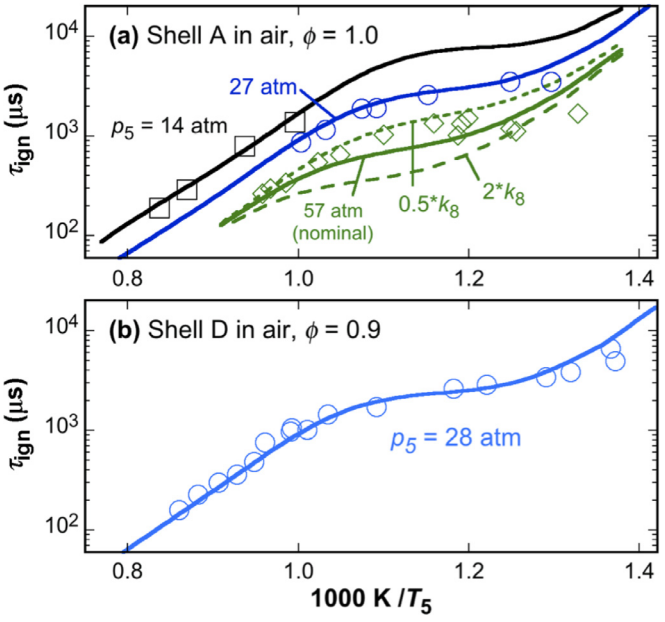

Fig. 5. Measured (symbols) and simulated (lines) ignition delay times of Shell A (a) and Shell D (b) in air. Long and short dashed line represent the k_8 sensitivity for simulated ignition delay time of Shell A at $p_5 = 57$ atm.

$$C_mH_{n-1} \rightarrow \gamma CH_4 + e_a(C_2H_4 + \lambda_3 C_3H_6 + \lambda_{4,i} i\text{-}C_4H_8) + b_a[\chi C_6H_6 + (1-\chi)C_7H_8] + \beta H + (1-\beta)CH_3 \quad \text{(R2b)}$$

where R = H, CH_3, OH, O_2, HO_2, and O. The reaction rate coefficients of (R2a) are set to be equal to those of corresponding reactions (R2-R7). The rate parameters of (R2b) are assumed to be equal to the sum of the β-scission rates of an equilibrated population of all *n*-octyl radical isomers. Tests show that these changes do not affect HyChem model predictions for the high-temperature experiments. The NTC and low-temperature chemistry submodel is introduced as follows:

$$C_mH_{n-1} + O_2 \leftrightarrow C_mH_{n-1}O_2 \quad \text{(R8)}$$

$$C_mH_{n-1}O_2 \leftrightarrow C_mH_{n-2}OOH \quad \text{(R9)}$$

$$C_mH_{n-2}OOH \leftrightarrow C_mH_{n-2} + HO_2 \quad \text{(R10)}$$

$$C_mH_{n-2} \rightarrow e_{al}(C_2H_4 + \lambda_3 C_3H_6 + \lambda_{4,i} i\text{-}C_4H_8) + b_{al}[\chi C_6H_6 + (1-\chi)C_7H_8] + \alpha H + (2-\alpha)CH_3 \quad \text{(R11)}$$

$$C_mH_{n-2}OOH + O_2 \leftrightarrow C_mH_{n-1}O_4 \quad \text{(R12)}$$

$$C_mH_{n-1}O_4 \leftrightarrow C_mH_{n-2}O_3 + OH \quad \text{(R13)}$$

$$C_mH_{n-2}O_3 \rightarrow CH_2O + CO + OH + e_k(C_2H_4 + \lambda_3 C_3H_6 + \lambda_{4,i} i\text{-}C_4H_8) + b_k[\chi C_6H_6 + (1-\chi)C_7H_8] + \alpha H + (2-\alpha)CH_3 \quad \text{(R14)}$$

As discussed earlier [32], reactions (R8–9) represents the addition of O_2 to the HC component "radical" producing the peroxyl radical RO_2, which isomerizes to the QOOH radical via H-atom shift. The hydroperoxy radical ($C_mH_{n-2}OOH$ or QOOH) exhibits two reaction channels: (1) decomposition to the unreactive HO_2 radical and the alkene form of the HC "molecule" (R10–11); (2) additional O_2 addition to form $C_mH_{n-1}O_4$ (OOQOOH) through (R12). The dissociation of OOQOOH produces the net chain branching effect by yielding the OH radical and ketohydroperoxide ($C_mH_{n-2}O_3$ or OQOOH), which is open to decomposition reaction leading to further chain branching (R14).

In the above formulation, the thermochemical data of the NTC-related pseudo-species, including $C_mH_{n-1}O_2$, $C_mH_{n-2}OOH$, $C_mH_{n-1}O_4$, and $C_mH_{n-2}O_3$, are estimated using the group additivity method. For example, the property value of $C_8H_{15}O_2$ (for Shell A) is calculated from the thermochemical property values of *n*-octane and its peroxy radical in JetSurF 1.0 [53]:

$$P(\text{ShellA}, C_8H_{15}O_2) = P(\text{ShellA}, C_8H_{16}) + P(C_8H_{17}O_2) - P(n\text{-}C_8H_{18})$$

where *P* is the specific heats, entropy, and enthalpy of formation at the standard state. The sensitivity on NTC-related thermochemical properties will be discussed in both the later part of the text and Supplementary Material (S7). The independent stoichiometric coefficients in reactions (R11) and (R14) are kept the same as those in (R1), and the dependent parameters e_{al}, b_{al}, e_k, b_k can be derived from elemental conservation in a similar manner to Eqs. (1)-(7). The rate parameters k_{8-14} are initially adopted from those of jet fuels in [32]. Selected rate parameters (k_8 and k_{14}) were adjusted within a factor of 5 from those of Jet A [32]. Figure 5 shows the complete set of measured and simulated ignition delay times under the same conditions as those shown in Fig. 3a and b. NTC behavior is noticeable starting at ~30 atm. It is evident that the model captures the NTC chemistry efficiently and accurately. Sensitivity analysis shows that the reaction of fuel radical *R* with O_2 producing RO_2 (R8), and the decomposition of ketohydroperoxide (R14) impact the ignition delay time over the temperature range of 700 to 1100 K the most. The rate constants of the two reactions are adjusted against only the 27 atm ignition delay time data for Shell A and 28 atm data for Shell D. This approach allows the reaction model to reproduce the ignition delay data at lower (14 atm) and higher (57 atm) pressures, providing more direct evidence that supports the extrapolative capability of the NTC-enabled HyChem with respect to pressure.

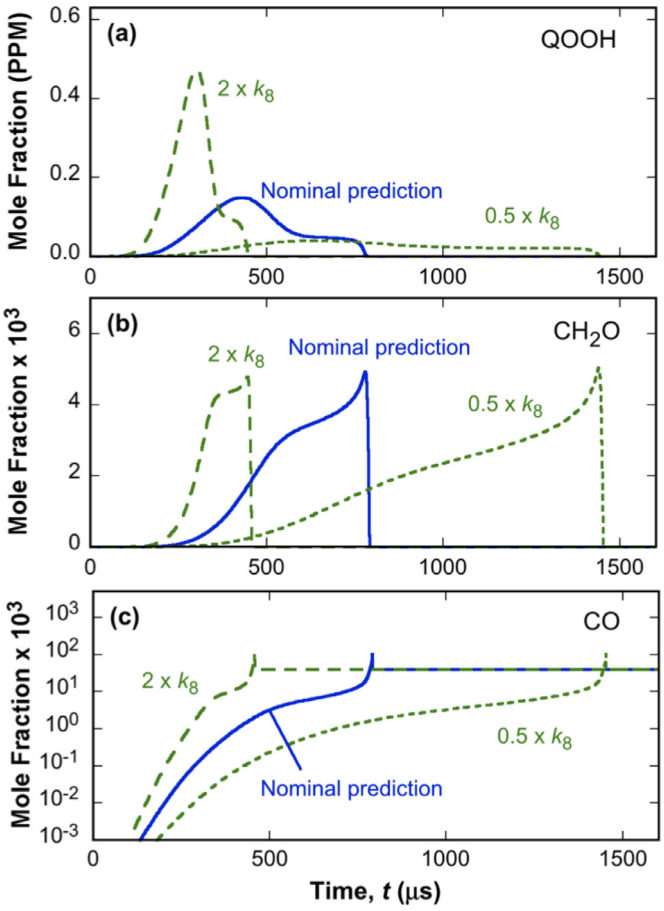

Fig. 6. Simulated QOOH (a), CH_2O (b), and CO (c) time histories for Shell A ignition at $T_5 = 875$ K at $p_5 = 57$ atm.

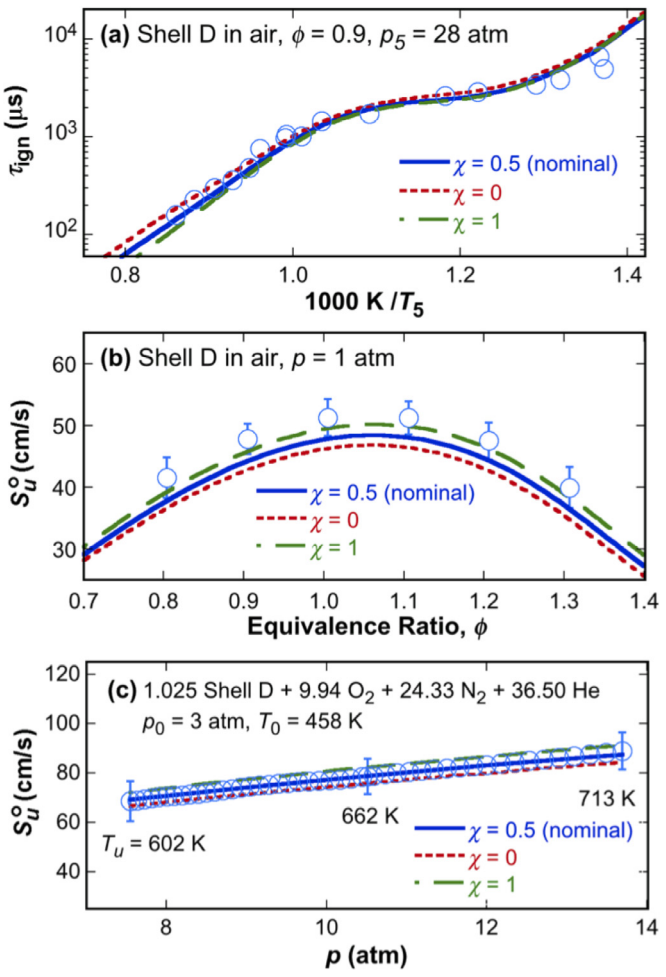

Fig. 7. Sensitivity of model predictions to the χ value. (a) Ignition delay times of Shell D in air; (b) laminar flame speeds of Shell D-air mixtures at ambient pressure and unburned gas temperature of 373 K; (c) laminar flame speeds of Shell D under the conditions shown. The T_u values marked in (c) are unburned mixture temperatures, and the flame pressures are indicated by the x-axis. T_0 and p_0 are initial temperature and pressure of the spherical chamber, which are not used in the simulation. Symbols are experimental data; lines are model predictions; the error bars representing 2-standard deviation of the data.

Additionally, we note that the ignition delay time prediction is sensitive to the thermochemical properties of species related to NTC chemistry [64]. In particular, Zádor et al. [65] reviewed and emphasized the features of the equilibrium of reaction (R8), the O_2 addition to fuel radical R. Here, we perform sensitivity analyses on the thermochemical data of RO_2 ($C_mH_{n-1}O_2$). It is found that within the conditions tested, the uncertainty of the equilibrium constant K_{p8} induced by the uncertainty in the RO_2 thermochemistry plays a negligible role in the ignition delay time predictions. Details and results of the sensitivity analyses are included in the Supplementary Material (Section S7, Fig. S11).

We note that the purpose of the current NTC extension is not about fitting the model parameters against the ignition delay time. A key question that needs to be addressed within the realm of HyChem is, what species should be considered as the target(s) for characterizing the NTC behavior of a fuel. As discussed in our jet fuel study [32], QOOH and CH_2O are the two key markers of the NTC activities. In addition to the sensitivity of the ignition delay with respect to k_8 depicted in Fig. 5a, we also perform a sensitivity analysis of the key species time histories with respect to k_8 in the same range of $\times 2$ and $\div 2$. Within this k_8 range, the variations of time histories of QOOH and CH_2O are drastic, as shown in Fig. 6a and b. Figure 6c also suggests that CO also exhibits a strong sensitivity in its time history to k_8. Considering the fact that the diagnostics of QOOH is exceedingly challenging, the results presented here suggest that both CH_2O and CO are viable candidates for use as the key NTC markers. Interestingly, our recent study [66] showed that CH_2O and CO may also be useful for reducing the HyChem model prediction uncertainty in high-temperature window of 1000–1100 K.

4.3. Sensitivity analysis of selected stoichiometric coefficient parameters

As we mentioned in Section 4.1, the χ value (the ratio of benzene concentration to the sum benzene and toluene concentrations) was estimated from previous jet fuel experiments. The sensitivity of model prediction to the χ value is presented in Fig. 7 for Shell D and Fig. S9 for Shell A. As seen, the variation of χ between 0 and 1 impacts the oxidation of Shell D to a limited extent, and such an effect is of relevance toward high temperature. The χ variation from 0 to 1 leads to $a \pm 3$ cm/s variation in the high-pressure flame speed. Such a variation is well within the 2σ uncertainty of the data. Figure S9 indicates that the impact of χ on the combustion predictions of Shell A is negligible, because of the small overall production of benzene and toluene from the fuel. Additional sensitivity tests on λ_3 are also presented in the Supplementary Material (Fig. S10), and a similar conclusion can be drawn.

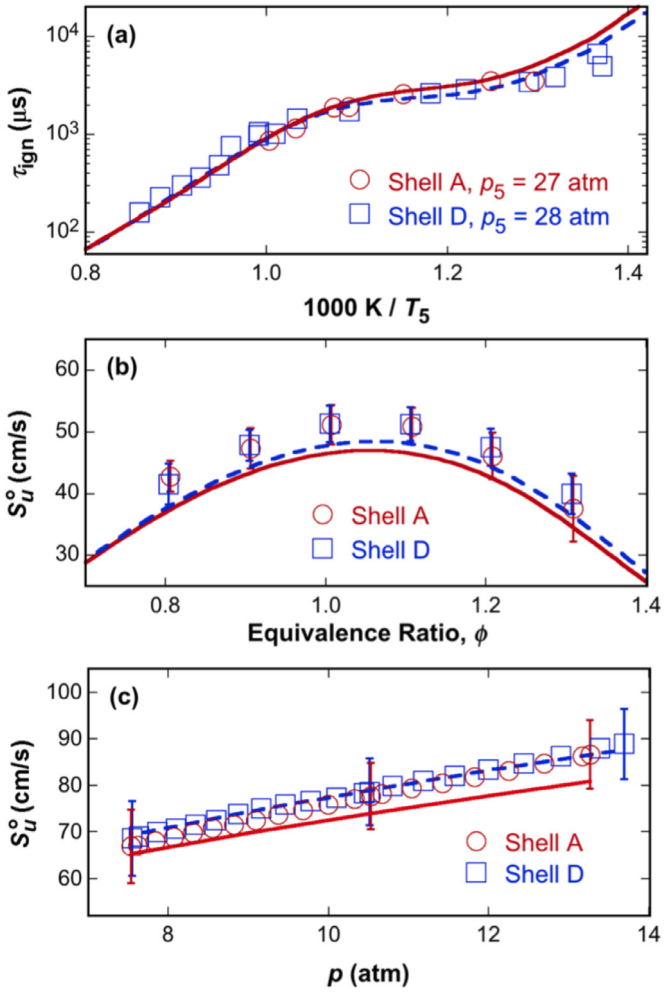

Fig. 8. Measured (symbols) and simulated (solid lines: Shell A, dashed lines: Shell D) of (a) shock-tube ignition delay times of fuel-air mixtures (Shell A: $\phi = 1.0$, Shell D: $\phi = 0.9$); (b) laminar flame speeds of fuel-air mixtures at ambient pressure and an unburned gas temperature of 373 K; (c) laminar flame speeds at elevated pressures with mixture compositions (mol): 1.003 Shell A+10.49 O_2 + 25.66 N_2 + 38.49 He ($\phi = 1.003$) and 1.025 Shell D+9.94 O_2 + 24.33 N_2 + 36.50 He ($\phi = 1.025$). See Fig. 3e and f for the unburned mixture temperatures. The error bars in (b) and (c) represent 2-standard deviations of the data.

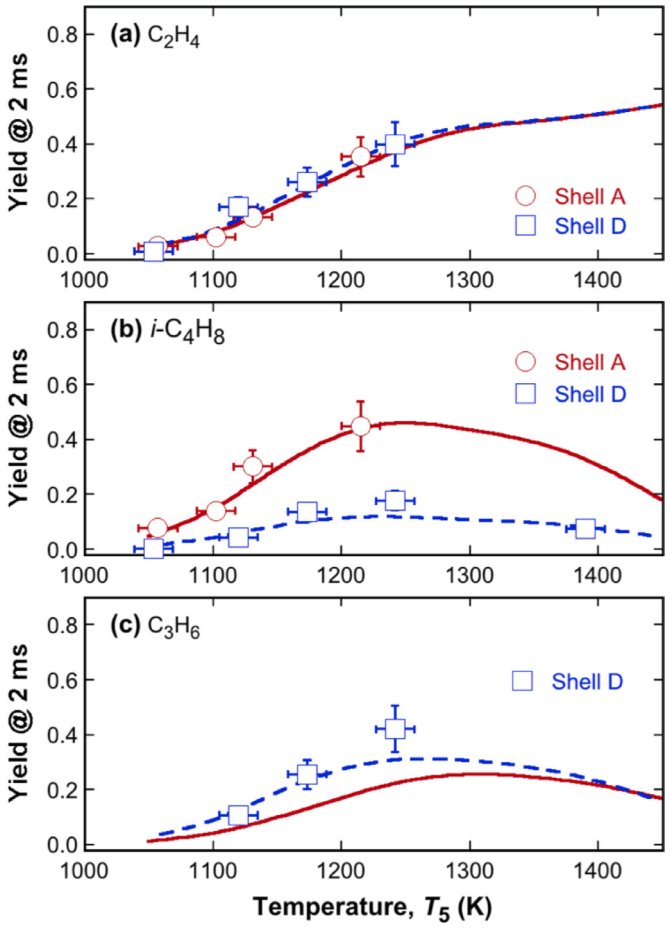

Fig. 9. Yields of (a) C_2H_4, (b) i-C_4H_8 and (c) C_3H_6 experimentally determined (symbols) and computed (solid lines: Shell A, dashed lines: Shell D) at 2 ms in shock tube pyrolysis of 0.8% of Shell A and Shell D in argon at $p_5 \sim 2$ atm. Horizontal and vertical error bars represent ± 15 K of temperature uncertainty and 2-standard deviation of the measured species concentrations.

4.4. Shell A vs. Shell D: understanding the small difference in their combustion properties

Shell D differs from Shell A quite drastically in the aromatic, *iso*-paraffin, and olefin contents (*cf*, Fig. 1). Shell A contains > 65% (mass) *iso*-paraffin, more than double of the *iso*-paraffin content in Shell D; the richest content in Shell D appears to be the aromatics (38.4% by mass) (see, Fig. 1 for additional detail). Suffice it to note that the composition difference of the two fuels does lead to differences in the high-temperature pyrolysis products. Yet despite these differences, the global combustion properties of the two fuels do not differ, at least within the statistical errors of the available experiment, as seen in Fig. 8.

The question is then, why the global combustion properties differ so little? To explore the answer to this question, we plot in Fig. 9 the yields of three key species (C_2H_4, C_3H_6, and i-C_4H_8), comparing the pyrolysis of Shell A and Shell D under a representative, comparable condition. Since the ethylene yield is the same between the two fuels (Fig. 9a), the difference in the global combustion properties can only be the result of differences in C_3H_6, i-C_4H_8, benzene and toluene production. While the two fuels have

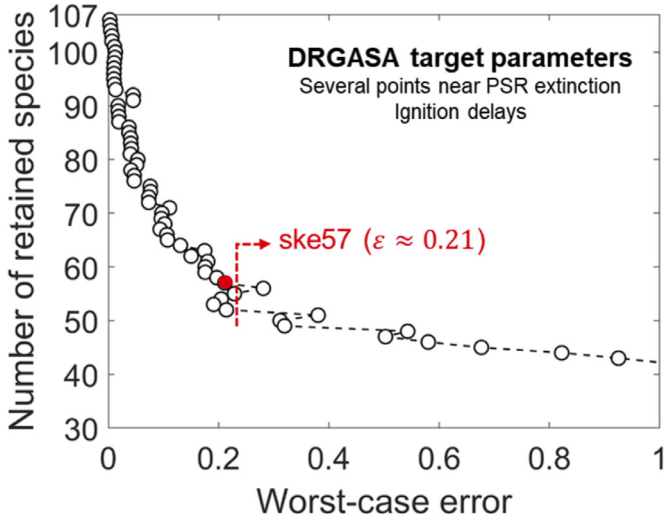

Fig. 10. Number of retained species as a function of the worst-case error in DRGASA for Shell A.

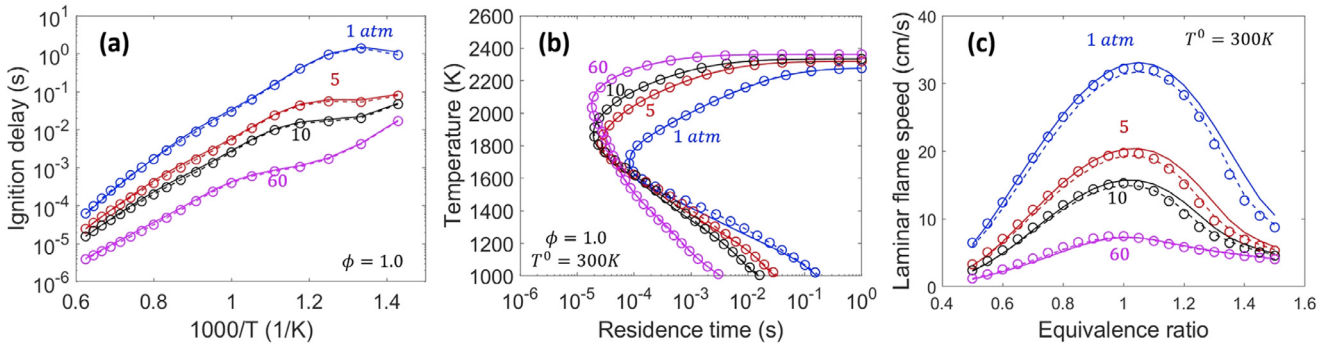

Fig. 11. Validation of the skeletal and reduced models for (a) ignition delay, (b) PSR extinction, and (c) laminar flame speed with free stream temperature of 300 K for Shell A/air. Detailed: solid lines, skeletal: dashed lines, reduced: symbols.

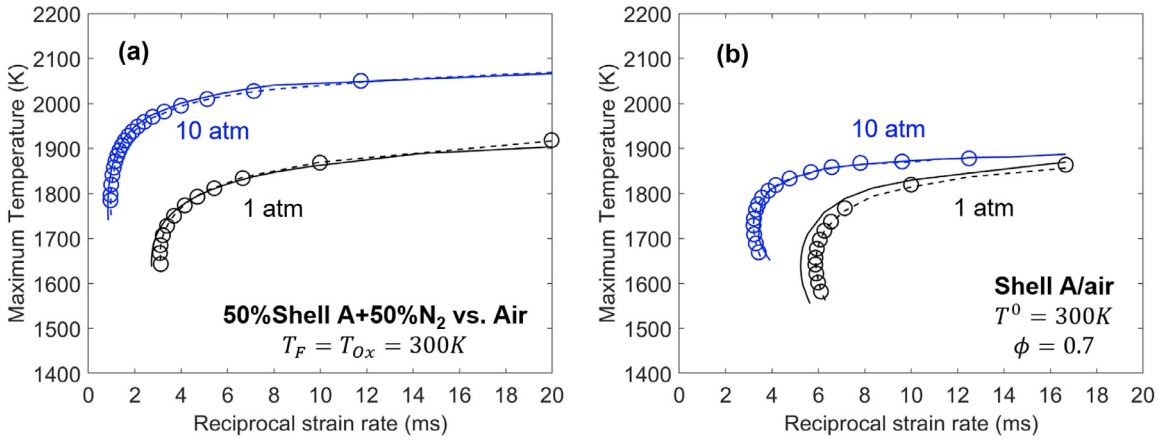

Fig. 12. Maximum temperature in (a) non-premixed counterflow flames of N_2-diluted Shell A (50% in mole) opposed to the air with temperatures of 300 K at both inlets, and (b) premixed counterflow flames with equivalence ratio of 0.7 and the free-stream temperature of 300 K, as a function of the reciprocal strain rate. Detailed: solid lines, skeletal: dashed lines, reduced: symbols.

nearly identical C_2H_4 production, Shell A produces more i-C_4H_8 and Shell D yields more C_3H_6. Additionally, Shell D produces substantially more benzene and toluene. The fact that the two fuels have nearly identical combustion property values suggest that the reactivities of the two sets of pyrolysis products are nearly the same – one that is dominated by i-C_4H_8, and the other dominated by aromatics and to an extent, C_3H_6. The respective fuel components that give rise to the two distinctive sets of the pyrolysis products are highly branched alkanes and aromatics (see, Fig. 1), both of which suppress the NTC activities.

4.5. Model reduction

The HyChem models are reduced for improved computational efficiency in CFD simulations, and the reduction results are demonstrated here with the Shell A model only, with more detailed validation results shown in the Supplementary Materials (S8). Skeletal reduction is first performed using the method of directed relation graph (DRG) with H radical as the starting species [67], followed by the DRG-aided sensitivity analysis (DRGASA) with perfectly stirred reactors (PSR) extinction profiles and auto-ignition delay time as target parameters [68]. Time-scale based reduction is then performed using the linearized quasi-steady-state approximations (LQSSA) [69]. Both reduction stages are based on reaction states sampled from auto-ignition and PSR, over pressure of 1–60 atm, equivalence ratio of 0.5–1.5, initial temperature of 700–1600 K for auto-ignition, and inlet temperature of 300 K for PSR. Note that reduced models based on both auto-ignition and PSR have been successfully extended to other flame conditions, such as laminar flame propagation and flame extinction [70]. The error tolerance is set to be 0.3 in DRG, resulting in a 107-species skeletal model for Shell A. The final skeletal model consists of 57 species by choosing the worst-case error to be about 0.21 based on the reduction curve shown in Fig. 10, as it is seen that the reduction error rapidly increases if any species are further eliminated.

In the timescale-based reduction stage, sixteen species are identified as global quasi-steady state (QSS) species using a method based on computational singular perturbation (CSP) [71] by specifying a worst-case relative error tolerance of about 0.1, and the final reduced model for Shell A consists of 41 species. The QSS species are hidden from the transport equations and their concentrations are analytically solved using internal algebraic equations when evaluating the reaction rates of the major species [69]. By following the same reduction procedure, a 55-species skeletal model and a 39-species reduced models for Shell D are obtained. Table 6 summarizes the number of species and reactions in detailed, skeletal, and reduced models for Shell A and D. All the reaction model files are available in the SM and can be accessed

Table 6
Number of species and reactions in detailed, skeletal, and reduced models.

Fuel	Reaction model	No. of species	No. of reactions
A	Detailed (original)	130	882
	Skeletal	57	354
	Reduced	41	354
D	Detailed (original)	130	882
	Skeletal	55	320
	Reduced	39	320

also through the link: https://web.stanford.edu/group/haiwanglab/HyChem/.

Figure 11 shows selected validation results for the skeletal and reduced models for Shell A for ignition delay, PSR extinction, and laminar flame speed. The worse-case errors are approximately 20% for ignition delay, 21% for PSR extinction, and approximately 3.7 cm/s for flame speed for rich mixtures and less than 1 cm/s for lean to stoichiometric mixtures. Figure 12 further compares the maximum temperature in non-premixed and premixed counterflow flames as a function of the reciprocal strain rate at pressure of 1 and 10 atm. The worst-case relative error in extinction strain rate is less than 15%. Similar validation results are obtained for Shell D as shown in the Supplementary Materials (S8).

5. Conclusions

In the present work, the HyChem approach was applied to the development of reaction models for two Shell gasoline fuels. The model parameters were derived using the species time history data obtained from shock tube pyrolysis experiment and laser diagnostic techniques. The reaction models were subsequently tested against ignition delay time and laminar flame speed over a wide range of conditions. The overall agreement between the HyChem model predictions and experiment was shown to be satisfactory. Combined with results obtained for a range of aviation and rocket fuels, we find the approach to be robust to modeling real-fuel combustion chemistry.

The result also supports the extrapolative capability of the NTC-enabled HyChem model over a wide range of pressures. Formaldehyde and carbon monoxide are found to be the most viable measurement targets for the NTC extension of the model. The sensitivities of model predictions to selected stoichiometric coefficient parameters were examined. The results show that in absence of direct measurements, even rough estimation of certain stoichiometric coefficients in the lumped reaction model imposes little to no effect on the model predictions. The absence of the combustion property variations due to fuel composition changes was examined to an extent. The results suggest that the respective fuel components (highly branched alkanes and aromatics) that suppress the NTC activities produce high-temperature pyrolytic products that exhibit nearly the same ignition and flame propagation properties for the two fuels tested. Lastly, we show that each NTC-enabled model may be reduced to about 40 species in size; and these reduced models are sufficient for making useful predictions of the entire set of combustion behaviors of real gasoline fuels.

Declaration of Competing Interest

The authors declare that they have no known competing financial interests or personal relationships that could have appeared to influence the work reported in this paper.

Acknowledgment

The work at Stanford University (RKH, HW) and University of Southern California (FNE) was supported by Shell Global Solutions. The work at UConn (TL) was supported by the US Air Force Office of Scientific Research (FA9550-15-1-0496).

Supplementary materials

Supplementary material associated with this article can be found, in the online version, at doi:10.1016/j.combustflame.2020.07.020.

References

[1] S.M. Sarathy, A. Farooq, G.T. Kalghatgi, Recent progress in gasoline surrogate fuels, Prog. Energy Combust. Sci. 65 (2018) 67–108.
[2] M.D. Boot, M. Tian, E.J. Hensen, S.M. Sarathy, Impact of fuel molecular structure on auto-ignition behavior–design rules for future high performance gasolines, Prog. Energy Combust. Sci. 60 (2017) 1–25.
[3] A. Violi, S. Yan, E. Eddings, A. Sarofim, S. Granata, T. Faravelli, E. Ranzi, Experimental formulation and kinetic model for JP-8 surrogate mixtures, Combust. Sci. Technol. 174 (2002) 399–417.
[4] F.L. Dryer, Chemical kinetic and combustion characteristics of transportation fuels, Proc. Combust. Inst. 35 (2015) 117–144.
[5] M. Colket, T. Edwards, S. Williams, N.P. Cernansky, D.L. Miller, F.N. Egolfopoulos, P. Lindstedt, K. Seshadri, F.L. Dryer, C.K. Law, D. Friend, D.B. Lenhert, H. Pitsch, A. Sarofim, M.D. Smooke, W. Tsang, Development of an experimental database and kinetic models for surrogate jet fuels, 45th AIAA Aerospace Sciences Meeting and Exhibit, 2007.
[6] W.J. Pitz, C.J. Mueller, Recent progress in the development of diesel surrogate fuels, Prog. Energy Combust. Sci. 37 (2011) 330–350.
[7] S. Dooley, S.H. Won, J. Heyne, T.I. Farouk, Y.G. Ju, F.L. Dryer, K. Kumar, X. Hui, C.J. Sung, H.W. Wang, M.A. Oehlschlaeger, V. Iyer, S. Iyer, T.A. Litzinger, R.J. Santoro, T. Malewicki, K. Brezinsky, The experimental evaluation of a methodology for surrogate fuel formulation to emulate gas phase combustion kinetic phenomena, Combust. Flame 159 (2012) 1444–1466.
[8] S. Dooley, S.H. Won, M. Chaos, J. Heyne, Y. Ju, F.L. Dryer, K. Kumar, C.J. Sung, H. Wang, M.A. Oehlschlaeger, R.J. Santoro, T.A. Litzinger, A jet fuel surrogate formulated by real fuel properties, Combust. Flame 157 (2010) 2333–2339.
[9] N. Morgan, A. Smallbone, A. Bhave, M. Kraft, R. Cracknell, G. Kalghatgi, Mapping surrogate gasoline compositions into RON/MON space, Combust. Flame 157 (2010) 1122–1131.
[10] C. Pera, V. Knop, Methodology to define gasoline surrogates dedicated to auto-ignition in engines, Fuel 96 (2012) 59–69.
[11] C.K. Westbrook, M. Mehl, W.J. Pitz, G. Kukkadapu, S. Wagnon, K. Zhang, Multi--fuel surrogate chemical kinetic mechanisms for real world applications, Phys. Chem. Chem. Phys. 20 (2018) 10588–10606.
[12] W.J. Pitz, N.P. Cernansky, F.L. Dryer, F. Egolfopoulos, J. Farrell, D.G. Friend, H. Pitsch, Development of an experimental database and chemical kinetic models for surrogate gasoline fuels, SAE Trans. (2007) 195–216.
[13] E. Ranzi, A wide-range kinetic modeling study of oxidation and combustion of transportation fuels and surrogate mixtures, Energy Fuel 20 (2006) 1024–1032.
[14] H.J. Curran, P. Gaffuri, W.J. Pitz, C.K. Westbrook, W.R. Leppard, Autoignition chemistry in a motored engine: an experimental and kinetic modeling study, Symp. (Int.) Combust. 26 (1996) 2669–2677.
[15] C. Morley, A fundamentally based correlation between alkane structure and octane number, Combust. Sci. Technol. 55 (1987) 115–123.
[16] C.K. Westbrook, J. Warnatz, W.J. Pitz, A detailed chemical kinetic reaction mechanism for the oxidation of *iso*-octane and *n*-heptane over an extended temperature range and its application to analysis of engine knock, Symp. (Int.) Combust. 22 (1989) 893–901.
[17] M. Mehl, T. Faravelli, F. Giavazzi, E. Ranzi, P. Scorletti, A. Tardani, D. Terna, Detailed chemistry promotes understanding of octane numbers and gasoline sensitivity, Energy Fuel 20 (2006) 2391–2398.
[18] B. Gauthier, D. Davidson, R. Hanson, Shock tube determination of ignition delay times in full-blend and surrogate fuel mixtures, Combust. Flame 139 (2004) 300–311.
[19] T. Javed, C. Lee, M. AlAbbad, K. Djebbi, M. Beshir, J. Badra, H. Curran, A. Farooq, Ignition studies of *n*-heptane/*iso*-octane/toluene blends, Combust. Flame 171 (2016) 223–233.
[20] G. Kalghatgi, H. Babiker, J. Badra, A simple method to predict knock using toluene, *n*-heptane and *iso*-octane blends (TPRF) as gasoline surrogates, SAE Int. J. Engines 8 (2015) 505–519.
[21] G. Kalghatgi, K. Morganti, I. Algunaibet, S.M. Sarathy, R. Dibble, Knock prediction using a simple model for ignition delay, SAE, 2016 No. 2016-01-0702Technical Paper.
[22] M. Mehl, W.J. Pitz, C.K. Westbrook, H.J. Curran, Kinetic modeling of gasoline surrogate components and mixtures under engine conditions, Proc. Combust. Inst. 33 (2011) 193–200.
[23] M. Mehl, J.-.Y. Chen, W.J. Pitz, S.M. Sarathy, C.K. Westbrook, An approach for formulating surrogates for gasoline with application toward a reduced surrogate mechanism for CFD engine modeling, Energy Fuel 25 (2011) 5215–5223.
[24] S.M. Sarathy, G. Kukkadapu, M. Mehl, W. Wang, T. Javed, S. Park, M.A. Oehlschlaeger, A. Farooq, W.J. Pitz, C.-J. Sung, Ignition of alkane-rich FACE gasoline fuels and their surrogate mixtures, Proc. Combust. Inst. 35 (2015) 249–257.
[25] S.M. Sarathy, G. Kukkadapu, M. Mehl, T. Javed, A. Ahmed, N. Naser, A. Tekawade, G. Kosiba, M. AlAbbad, E. Singh, Compositional effects on the ignition of FACE gasolines, Combust. Flame 169 (2016) 171–193.
[26] A. Ahmed, G. Goteng, V.S. Shankar, K. Al-Qurashi, W.L. Roberts, S.M. Sarathy, A computational methodology for formulating gasoline surrogate fuels with accurate physical and chemical kinetic properties, Fuel 143 (2015) 290–300.
[27] C. Lee, A. Ahmed, E.F. Nasir, J. Badra, G. Kalghatgi, S.M. Sarathy, H. Curran, A. Farooq, Autoignition characteristics of oxygenated gasolines, Combust. Flame 186 (2017) 114–128.
[28] C.V. Naik, K. Puduppakkam, C. Wang, J. Kottalam, L. Liang, D. Hodgson, E. Meeks, Applying detailed kinetics to realistic engine simulation: the surro-

gate blend optimizer and mechanism reduction strategies, SAE Int. J. Engines 3 (2010) 241–259.
[29] K.V. Puduppakkam, L. Liang, C.V. Naik, E. Meeks, S.L. Kokjohn, R.D. Reitz, Use of detailed kinetics and advanced chemistry-solution techniques in CFD to investigate dual-fuel engine concepts, SAE Int. J. Engines 4 (2011) 1127–1149.
[30] L. Cai, H. Pitsch, Optimized chemical mechanism for combustion of gasoline surrogate fuels, Combust. Flame 162 (2015) 1623–1637.
[31] H. Wang, R. Xu,, K. Wang, C.T. Bowman, R.K. Hanson, D.F. Davidson, K. Brezinsky, F.N. Egolfopoulos, A physics-based approach to modeling real-fuel combustion chemistry – I. Evidence from experiments, and thermodynamic, chemical kinetic and statistical considerations, Combust. Flame 193 (2018) 502–519.
[32] R. Xu, K. Wang, S. Banerjee, J. Shao, T. Parise, Y. Zhu, S. Wang, A. Movaghar, D.J. Lee, R. Zhao, X. Han, Y. Gao, T. Lu, K. Brezinsky, F.N. Egolfopoulos, D.F. Davidson, R.K. Hanson, C.T. Bowman, H. Wang, A physics-based approach to modeling real-fuel combustion chemistry – II. Reaction kinetic models of jet and rocket fuels, Combust. Flame 193 (2018) 520–537.
[33] E. Ranzi, T. Faravelli, P. Gaffuri, A. Sogaro, Low-temperature combustion: automatic generation of primary oxidation reactions and lumping procedures,, Combust. Flame 102 (1995) 179–192.
[34] E. Ranzi, M. Dente, A. Goldaniga, G. Bozzano, T. Faravelli, Lumping procedures in detailed kinetic modeling of gasification, pyrolysis, partial oxidation and combustion of hydrocarbon mixtures, Prog. Energy Combust. Sci. 27 (2001) 99–139.
[35] A. Stagni, A. Cuoci, A. Frassoldati, T. Faravelli, E. Ranzi, Lumping and reduction of detailed kinetic schemes: an effective coupling, Ind. Eng. Chem. Res. 53 (2013) 9004–9016.
[36] R. Xu, H. Wang, Principle of large component number in multicomponent fuel combustion–a Monte Carlo study, Proc. Combust. Inst. 37 (2019) 613–620.
[37] X. You, F.N. Egolfopoulos, H. Wang, Detailed and simplified kinetic models of *n*-dodecane oxidation: the role of fuel cracking in aliphatic hydrocarbon combustion, Proc. Combust. Inst. 32 (2009) 403–410.
[38] K. Wang, C.T. Bowman, H. Wang, Kinetic analysis of distinct product generation in oxidative pyrolysis of four octane isomers, Proc. Combust. Inst. 37 (2019) 531–538.
[39] Y. Tao, R. Xu, K. Wang, J. Shao, S.E. Johnson, A. Movaghar, X. Han, J.-W. Park, T. Lu, K. Brezinsky, F.N. Egolfopoulos, D.F. Davidson, R.K. Hanson, C.T. Bowman, H. Wang, A physics-based approach to modeling real-fuel combustion chemistry – III. Reaction kinetic model of JP10, Combust. Flame 198 (2018) 466–476.
[40] K. Wang, R. Xu, T. Parise, J. Shao, A. Movaghar, D.J. Lee, J.-W. Park, Y. Gao, T. Lu, F.N. Egolfopoulos, D.F. Davidson, R.K. Hanson, C.T. Bowman, H. Wang, A physics-based approach to modeling real-fuel combustion chemistry – IV. HyChem modeling of combustion kinetics of a bio-derived jet fuel and its blends with a conventional Jet A, Combust. Flame 198 (2018) 477–489.
[41] L. Esclapez, P.C. Ma, E. Mayhew, R. Xu, S. Stouffer, T. Lee, H. Wang, M. Ihme, Fuel effects on lean blow-out in a realistic gas turbine combustor, Combust. Flame 181 (2017) 82–99.
[42] A. Felden, L. Esclapez, H.Wang Riber, B. Cuenot, Including real fuel chemistry in large-Eddy simulations, Combust. Flame 193 (2018) 397–416.
[43] D. Davidson, Y. Zhu, J. Shao, R. Hanson, Ignition delay time correlations for distillate fuels, Fuel 187 (2017) 26–32.
[44] T. Parise, D. Davidson, R. Hanson, Shock tube/laser absorption measurements of the pyrolysis of a bimodal test fuel, Proc. Combust. Inst. 36 (2017) 281–288.
[45] Y. Wang, A. Holley, C. Ji, F. Egolfopoulos, T. Tsotsis, H. Curran, Propagation and extinction of premixed dimethyl-ether/air flames, Proc. Combust. Inst. 32 (2009) 1035–1042.
[46] C. Xiouris, T. Ye, J. Jayachandran, F.N. Egolfopoulos, Laminar flame speeds under engine-relevant conditions: uncertainty quantification and minimization in spherically expanding flame experiments, Combust. Flame 163 (2016) 270–283.
[47] A. Movaghar, R. Lawson, F.N. Egolfopoulos, Confined spherically expanding flame method for measuring laminar flame speeds: revisiting the assumptions and application to C_1-C_4 hydrocarbon flames, Combust. Flame 212 (2020) 79–92.
[48] C. Liu, Z. Li, H. Wang, Drag force and transport property of a small cylinder in free molecule flow: a gas-kinetic theory analysis, Phys. Rev. E 94 (2016) 023102.
[49] C. Liu, W.S. McGivern, J.A. Manion, H. Wang, Theory and experiment of binary diffusion coefficient of *n*-alkanes in dilute gases, J. Phys. Chem. A 120 (2016) 8065–8074.
[50] C. Liu, R. Zhao, R. Xu, F.N. Egolfopoulos, H. Wang, Binary diffusion coefficients and non-premixed flames extinction of long-chain alkanes, Proc. Combust. Inst. 36 (2017) 1523–1530.
[51] H. Wang, X. You, A. Joshi, S.G. Davis, A. Laskin, F.N. Egolfopoulos, C.K. Law, USC Mech Version II. High-Temperature Combustion Reaction Model of H_2/CO/C_1-C_4 Compounds. http://ignis.usc.edu/USC_Mech_II.htm, 2007.
[52] W.K. Metcalfe, S.M. Burke, S.S. Ahmed, H.J. Curran, A hierarchical and comparative kinetic modeling study of C_1-C_2 hydrocarbon and oxygenated fuels, Int. J. Chem. Kinet. 45 (2013) 638–675.
[53] B. Sirjean, E. Dames, D.A. Sheen, X. You, C. Sung, A.T. Holley, F.N. Egolfopoulos, H. Wang, S.S. Vasu, D.F. Davidson, R.K. Hanson, H. Pitsch, C.T. Bowman, A. Kelley, C.K. Law, W. Tsang, N.P. Cernansky, D.L. Miller, A. Violi, N.P. Lindstedt, A high-temperature chemical kinetic model of *n*-alkane oxidation, JetSurF version 1.0, September 15, 2019, http://web.stanford.edu/group/haiwanglab/JetSurF/JetSurF1.0/index.html.
[54] H. Wang, E. Dames, B. Sirjean, D.A. Sheen, R. Tangko, A. Violi, J.Y.W. Lai, F.N. Egolfopoulos, D.F. Davidson, R.K. Hanson, C.T. Bowman, C.K. Law, W. Tsang, N.P. Cernansky, D.L. Miller, R.P. Lindstedt, A high-temperature chemical kinetic model of *n*-alkane (up to *n*-dodecane), cyclohexane, and methyl-, ethyl-, *n*-propyl and *n*-butyl-cyclohexane oxidation at high temperatures, JetSurF, version 2.0, September 19, 2010, http://web.stanford.edu/group/haiwanglab/JetSurF/JetSurF2.0/index.html.
[55] R.J. Kee, F.M. Rupley, J.A. Miller, Chemkin-II: a Fortran chemical kinetics package for the analysis of gas-phase chemical kinetics, Sandia National Laboratories, Report No. SAND-89-8009, 1989.
[56] A.E. Lutz, R.J. Kee, J.A. Miller, SENKIN: a FORTRAN program for predicting homogeneous gas phase chemical kinetics with sensitivity analysis, Sandia National Laboratories, Report No. SAND-87-8248, 1988.
[57] G.P. Smith, C. Park, J. Luque, A note on chemiluminescence in low-pressure hydrogen and methane–nitrous oxide flames, Combust. Flame 140 (2005) 385–389.
[58] G.P. Smith, J. Luque, C. Park, J.B. Jeffries, D.R. Crosley, Low pressure flame determinations of rate constants for OH(A) and CH(A) chemiluminescence, Combust. Flame 131 (2002) 59–69.
[59] M. Tamura, P.A. Berg, J.E. Harrington, J. Luque, J.B. Jeffries, G.P. Smith, D.R. Crosley, Collisional quenching of CH(A), OH(A), and NO(A) in low pressure hydrocarbon flames, Combust. Flame 114 (1998) 502–514.
[60] P. Hogan, D. Davis, Electronic quenching and vibrational relaxation of the OH ($A^2\Sigma^+$, ν'=1) state, J. Chem. Phys. 62 (1975) 4574–4576.
[61] R.J. Kee, J.F. Grcar, M.D. Smooke, J. Miller, E. Meeks, PREMIX: a Fortran program for modeling steady laminar one-dimensional premixed flames, Sandia National Laboratories, Report No. SAND-85-8249, 1985.
[62] R. Choudhary, J. Shao, D.F. Davidson, R.K. Hanson, Personal Communication, 2019.
[63] G. Bikas, N. Peters, Kinetic modelling of *n*-decane combustion and autoignition: modeling combustion of *n*-decane, Combust. Flame 126 (2001) 1456–1475.
[64] H.J. Curran, Developing detailed chemical kinetic mechanisms for fuel combustion, Proc. Combust. Inst. 37 (2019) 57–81.
[65] J. Zádor, C.A. Taatjes, R.X. Fernandes, Kinetics of elementary reactions in low-temperature autoignition chemistry, Prog. Energy Combust. Sci. 37 (2011) 371–421.
[66] R. Xu, H. Wang, A physics-based approach to modeling real-fuel combustion chemistry – VII. Relationship between speciation measurement and reaction model accuracy, Combust. Flame (2020) submitted.
[67] T. Lu, C.K. Law, A directed relation graph method for mechanism reduction, Proc. Combust. Inst. 30 (2005) 1333–1341.
[68] X. Zheng, T. Lu, C. Law, Experimental counterflow ignition temperatures and reaction mechanisms of 1, 3-butadiene, Proc. Combust. Inst. 31 (2007) 367–375.
[69] T. Lu, C.K. Law, Systematic approach to obtain analytic solutions of quasi steady state species in reduced mechanisms, J. Phys. Chem. A 110 (2006) 13202–13208.
[70] T. Lu, C.K. Law, Toward accommodating realistic fuel chemistry in large-scale computations, Prog. Energy Combust. Sci. 35 (2009) 192–215.
[71] T. Lu, C.K. Law, A criterion based on computational singular perturbation for the identification of quasi steady state species: a reduced mechanism for methane oxidation with NO chemistry, Combust. Flame 154 (2008) 761–774.